Insights into the bilayer-mediated toppling mechanism of a folate-specific ECF transporter by cryo-EM

Thangaratnarajah, Chancievan; Rheinberger, Jan; Paulino, Cristina; Slotboom, Dirk J

Published in:
Proceedings of the National Academy of Sciences of the United States of America

DOI:
10.1073/pnas.2105014118

Publication date:
2021

Main Manuscript for

Insights into the bilayer-mediated toppling mechanism of a folate-specific ECF transporter by cryo-EM.

Chancievan Thangaratnarajah[1,2], Jan Rheinberger[1,2], Cristina Paulino[1,2]*, Dirk J. Slotboom[1]*

[1] University of Groningen, Faculty of Science and Engineering, Groningen Biomolecular Sciences and Biotechnology, Membrane Enzymology Group, Nijenborgh 4, 9747 AG, Groningen, Netherlands.

[2] University of Groningen, Faculty of Science and Engineering, Groningen Biomolecular Sciences and Biotechnology, Electron Microscopy Group, Nijenborgh 4, 9747 AG, Groningen, Netherlands.

* Dirk J. Slotboom & Cristina Paulino

Email: d.j.slotboom@rug.nl & c.paulino@rug.nl

Author Contributions: C.T, C.P. and D.J.S. designed experiments. C.T. performed all experiments. J.R. advised with data acquisition and image processing, and collected the cryo-EM data of ECF-FolT2 in detergent micelles. C.P. and D.J.S. supervised the project. C.T., C.P. and D.J.S. interpreted the data and wrote the manuscript. All authors read and revised the manuscript.

Competing Interest Statement: The authors declare no competing interests.

Classification: Biological sciences – Biochemistry

Keywords: membrane deformation, membrane protein, lipid nanodiscs, ABC transporter, cryo-EM

This PDF file includes:

Main Text
Figures 1 to 4

Abstract

Energy-Coupling Factor (ECF)-type transporters are small asymmetric membrane protein complexes (~115 kDa), which consist of a membrane-embedded substrate binding protein (S-component) and a tripartite ATP-hydrolyzing module (ECF module). They import micronutrients into bacterial cells and have been proposed to use a highly unusual transport mechanism, in which the substrate is dragged across the membrane by a toppling motion of the S-component. However, it remains unclear how the lipid bilayer could accommodate such a movement. Here we used cryo-EM at 200-kV to determine structures of a folate-specific ECF transporter in lipid nanodiscs and detergent micelles at 2.7 and 3.4-Å resolution, respectively. The structures reveal an irregularly shaped bilayer environment around the membrane embedded complex, and suggest that toppling of the S-component is facilitated by protein-induced membrane deformations. In this way, structural remodeling of the lipid bilayer environment is exploited to guide the transport process.

Significance Statement

Gram-positive bacteria that lack partial or complete biosynthesis pathways for micronutrients such as vitamins, use a class of membrane proteins to acquire them from the environment. These membrane proteins are called ECF transporters and function in an unusual way. A membrane-embedded substrate-binding protein rotates within the membrane to bring a molecule from the outside to the inside of the cell. It was however not clear how this motion can occur within a lipid environment. We use cryo-EM at 200-kV to visualise an ECF transporter within a lipid environment. The transporter causes deformations to the surrounding lipid environment. These insights offer an explanation how changes of the lipid environment enable such a motion in the transport process.

Main text

Introduction

Energy-Coupling Factor (ECF)-type transporters are membrane protein complexes that belong to the superfamily of ATP binding cassette transporters (ABC), where they form the phylogenetically, mechanistically and structurally distinct type III clade (1). A full ECF complex is formed by a minimum of four polypeptide chains or domains: two cytosolic nucleotide-binding proteins (EcfA and EcfA'), a membrane-embedded scaffold protein (EcfT) and a membrane-embedded substrate binding protein (S-component). The former three proteins form a tripartite module of ~ 93 kDa (named the energising or ECF module), while the S-component of ~ 19 kDa can be either associated with the ECF module ("full complex"), or be present in the membrane as a solitary protein. ECF transporter complexes catalyse the uptake of micronutrients such as vitamins and transition metals in bacteria and their substrate specificity is mediated by a different S-component for each substrate (2, 3). X-ray crystal structures suggest that the S-component must topple within the membrane to bring the substrate from the outside to the inside of the cell (3–5). Coarse-grained molecular dynamics simulations have indicated that the membrane bends and thins near the ECF module, providing a favourable environment for the S-component to topple within the lipid bilayer (5). However, experimental evidence for membrane deformations around ECF transporter complexes, required to substantiate this idea, is lacking. Most X-ray crystallisation methods use detergent-solubilised proteins, rendering a direct visualising of the bilayer environment, and consequently the correct positioning of the protein bilayer, impossible (3, 4, 6–9). Therefore, structures of ECF transporter complexes embedded in a more native environment are required to understand their interplay with the lipid bilayer. In this context, single-particle analysis by cryogenic electron microscopy (cryo-EM) has shown to be a suitable method to study the role of membrane remodelling with respect to the function of membrane proteins (10–17).
Here, we present the cryo-EM structures of the folate-specific ECF transporter complex (ECF-FolT2) in the inward-facing apo conformation at an overall resolution of 2.7 Å and 3.4 Å, with better

resolved local regions allowing to model water molecules. The cryo-EM structures obtained in lipid nanodiscs and detergent micelles reveal protein-lipid interactions and deformations of the surrounding environment, providing experimental evidence for a bilayer mediated toppling mechanism. With a total molecular weight of around 115 kDa for the full complex and the absence of symmetry, ECF transporter complexes are challenging targets for cryo-EM. We demonstrate that cryo-EM reconstructions at better than 3 Å resolution of such small asymmetric membrane proteins from data obtained with a 200-kV cryogenic transmission electron microscope (cryo-TEM) is conceivable.

Results

Cryo-EM structure of ECF-FolT2 in lipid nanodiscs

We chose the folate-specific transporter complex ECF-FolT2 from *Lactobacillus delbrueckii* for analysis by cryo-EM, because this transporter has been characterised previously by X-ray crystallography, liposome-based uptake assays and coarse-grained molecular dynamics simulations, which provides a context for interpretation of the data (3–5). ECF-FolT2 was purified in n-dodecyl-β-D-maltopyranoside (DDM) micelles as described previously (4) (*SI Appendix*, Fig. S1 *A*), and subsequently reconstituted into lipid nanodiscs. *Escherichia coli* polar lipid extracts were chosen for the reconstitution, since the transporter displayed high transport activities in liposomes composed of these lipids (4, 5). For the formation of lipid nanodiscs, we selected the membrane scaffold protein 2N2 (MSP2N2), as it can form lipid nanodiscs with diameters of approximately 16 nm (18). This size would be large enough to ensure that the membrane-embedded domains of the complex are accommodated without size constraints, which might otherwise hinder conformational changes to occur.

To find suitable reconstitution conditions, we varied the amounts of lipids while keeping the ratio of the transport complex to membrane scaffold protein constant, and assessed the quality of the nanodisc reconstitutions by size-exclusion chromatography (*SI Appendix,* Fig. S1 *B*). The elution volumes of the complexes indicate that higher lipid content resulted in lipid nanodiscs of increasing diameter, while peak broadening suggests that higher lipid to protein ratios led to more heterogeneous size distribution of the protein-lipid nanodisc complexes. This was indeed observed in a cryo-EM dataset collected with the transporter reconstituted at a molar ratio of 1:5:500 protein : MSP2N2 : lipids (*SI Appendix,* Fig. S1 *C*). Already at a 2D classification level, heterogeneity in the size of the lipid nanodiscs surrounding the transporter was evident. The 3D classification results showed that the transporter is enclosed by elliptical lipid nanodiscs, ranging from ~98 to 123 Å in the longest dimension. The refinement of the two dominant classes however only yielded reconstructions between 9 and 10 Å resolution.

We reasoned that higher resolution reconstruction might be obtained in single-particle analysis using ECF-FolT2 reconstituted at a molar ratio of 1:5:250 protein : MSP2N2 : lipids, because of the more homogenous sample behaviour by size-exclusion chromatography (*SI Appendix,* Fig. S1 *B,D*). SDS-PAGE analysis and ATPase activity assays confirmed that a full-length functional protein was reconstituted into lipid nanodiscs (*SI Appendix,* Fig. S1 *D,E*). Cryo-EM data acquisition was optimised by selection of regions with an even particle distribution based on sample thickness, using an in-house written script (*SI Appendix,* Fig. S2 *A*) (19). While we generally target regions with a sample thickness of 20-40 nm for data collection, the dataset for the ECF complex in nanodiscs was acquired in the 30-50 nm range. This however did not affect the quality of the data with 90 % of the cryo-EM images revealing CTF resolution estimations of 4 Å or better (*SI Appendix,* Fig. S2 *B*). The 2D class averages displayed relatively uniform lipid nanodisc dimensions along with visible secondary structure elements, and distinct views corresponding to ECF-FolT2 (*SI Appendix,* Fig. S2 *C*).

The lipid nanodisc is elliptical in shape and approximately 88 x 76 Å in size. The relative small size is likely the result of the lipid to protein ratio used during the reconstitution, and is in agreement

with the observation that the membrane scaffold protein MSP2N2 forms lipid nanodiscs with a diameter of approximately 16 nm at higher lipid to protein ratios, while smaller lipid nanodiscs are formed at lower ratios (18). Notably, smaller than 16 nm lipid nanodisc diameters with MSP2N2 were also observed in other structures where low amounts of lipids were used such as the archaeal glutamate transporter homolog from *Thermococcus kodakarensis* (12). This elliptical (rather than circular) shape of the nanodiscs is most likely dictated by the reconstituted protein, which is elliptical with dimensions of approximately 60 x 30 Å within the plane of membrane.

In the end, we obtained a reconstruction of ECF-FolT2 in lipid nanodiscs at 2.7 Å resolution (*SI Appendix,* Fig. S3 *A-D*, Table S1), with better resolved local regions allowing an unambiguous fit of the atomic coordinates (Fig. 1*A*) and several water molecules (*SI Appendix,* Fig. S4 *A*). At present, this is the highest resolution structure for an ECF transporter complex, and in fact the highest reported resolution for a small asymmetric membrane protein with cryo-EM data acquired with a 200-kV cryo-TEM.

The inward-facing apo state is a structurally stable conformation

ECF-FolT2 in lipid nanodiscs adopts an inward-facing apo conformation, where the S-component FolT2 assumes a substrate-free 'toppled' state with both nucleotide-binding proteins in the open and nucleotide-free conformation. This conformation resembles the post-substrate-release state (3, 4, 6–9) obtained in previous crystallographic studies on ECF transporter complexes (Fig. 1*A*), showing that the inward-facing apo conformation represents a structurally stable conformation in a near native and non-native environments.

Despite the overall similarity, there are pronounced differences in the interactions between the subunits of the complex. While the core of both nucleotide-binding proteins, as well as the coupling helices of the scaffold protein EcfT align overall well between the cryo-EM and X-ray crystal structures of ECF-FolT2 (4) (rmsd 1.5 Å, *SI Appendix,* Fig. S4 *B,C*), deviations are seen in the C-terminal part of both nucleotide-binding proteins and in the membrane protein components of the complex (*SI Appendix,* Fig. S4 *B,C*).

Compared to the two X-ray crystal structures of ECF-FolT2, the transmembrane helices (TMH) of EcfT have hinged towards FolT2 with the pivot point corresponding to a conserved Pro71 (*SI Appendix,* Fig. S4 *D*). As a consequence, FolT2 is packed more tightly against the coupling helices in the cryo-EM structures compared to both X-ray crystal structures (*SI Appendix,* Fig. S4 *E*). This difference in domain conformation is translated into altered interactions. A π-interaction between FolT2 and EcfT is formed between Tyr134 in FolT2 and Phe116 in EcfT (Fig. 1*B*), which was not observed previously in the crystal structures (Fig. 1*C*). Also interactions of loops L3 and L5 in FolT2 with TMH4 and TMH3 in EcfT, respectively, are lost when compared to the AMP-PNP-bound structure (Fig. 1*B,C*).

Additional interactions are formed between the carboxy-terminal tail of FolT2 and the nucleotide-binding protein EcfA', which were also not observed in the X-ray crystal structures (Fig. 1*D,E*). Here, two positively charged residues Arg174 and Lys175 in FolT2 are rotated towards and extend into the space between both nucleotide-binding proteins (Fig. 1D, *SI Appendix,* Fig. S4 *E*). The arginine residue forms interactions with the backbone of residues Asp145 and Leu146 in EcfA', while the side chain of the same aspartate residue in EcfA' forms an interaction with the backbone of Arg174 in FolT2 (Fig. 1*D*). Such interactions are not observed in the AMP-PNP-bound structure as the two positively charged residues in FolT2 are rotated away from EcfA' (Fig. 1*E*). Notably, the surfaces of FolT2 and EcfA' in this region are highly complementary in terms of shape and surface charges (*SI Appendix,* Fig. S4 *F*).

The modular nature of ECF transporter complexes requires a degree of flexibility to facilitate the docking and toppling of the S-components. The differences in the interactions observed between EcfT and the S-component are in agreement with the dynamic nature of the transmembrane region

of EcfT (3, 4, 6, 9), which is an important feature to accommodate different S-components and to facilitate the toppling of the substrate-bound S-component during the transport cycle (3–6). Although unrelated in sequence and in substrate specificities, different S-components have a common structural fold and can dock onto the same ECF module (3, 4, 6, 20, 21). Interestingly, a previously unnoticed common feature is the presence of positively charged residues at the carboxy-terminal end of different S-components (*SI Appendix,* Fig. S5 *A*). Analysis of a recent crystal structure of the pantothenate-specific ECF transporter complex (ECF-PanT) (3), which uses the same ECF module as FolT2, indeed revealed two positively charged residues, Arg203 and Lys205 that point into the space between both nucleotide binding proteins (*SI Appendix,* Fig. S5 *B*). Although not previously described, they form a similar interaction as observed in the here reported cryo-EM structure of ECF-FolT2. In ECF-PanT, the arginine residue in PanT interacts with the backbone of residue Phe144 in EcfA', while Asp145 in EcfA' forms an interaction with Lys202 in PanT (*SI Appendix,* Fig. S5 *C*). It is likely that other S-components form similar interactions, contributing to their ability to use of the same ECF module.

Protein-mediated deformation of the surrounding environment

One of the advantages of cryo-EM is that apart from the target protein, also its surrounding environment is resolved. Visualisation of the lipid nanodisc surrounding ECF-FolT2 makes it possible to define the lipid bilayer boundaries and potential bilayer deformations (Fig. 2). The membrane components EcfT and FolT2 form together a highly asymmetrical structure that is inserted into the lipid nanodisc. The two nucleotide-binding proteins EcfA and EcfA' protrude from the lipid nanodisc on the side corresponding to the cytoplasmic side. On the opposite side corresponding to the extracellular side, neither EcfT nor FolT2 have regions that protrude from the lipid nanodisc. Notably, the long and predominantly hydrophobic loop connecting TMH3 and TMH4 in EcfT is embedded within the boundary of the lipid nanodisc, in contrast to the more exposed conformation modelled in the crystal structure (Fig. 2, *SI Appendix,* Fig. S4 *C*).

The lipid nanodisc is deformed with non-uniform in thickness, and not shaped symmetrically. While the bulk of the nanodisc displays a thickness of approximately 32 - 33 Å, it is substantially thinner near the interface between EcfT and FolT2 (Fig. 2). At the level of the exit path for folate to the cytosol, which is lined by the tip of loop L1 of FolT2 and a conserved Pro71 in TMH3 of EcfT, a thinning to approximately 28 Å is observed (Fig. 2*A*). An even stronger thinning of the lipid nanodisc to approximately 23 Å is observed on the opposite side, where the cytoplasmic face of FolT2 rests on the coupling helices, as well as around the terminal regions of coupling helices 1-3 and the amino-terminal part of the loop connecting coupling helix 3 with TMH5 of EcfT (Fig. 2*B*).

It could be argued that the observed bilayer deformations might be caused by a poor fit of the transporter in the nanodisc or by direct interactions with the scaffold protein. However, the surface area of the bilayer in the nanodiscs is much larger than the footprint of the membrane components of the transporter (~ 3800 Å^2 vs ~ 3100 Å^2). In addition, an argument against the deformation due to interactions between the transporter and the scaffold protein is the lack of defined density for the membrane scaffold protein. Yet, to test whether nanodisc constraints might contribute to the observed deformation, we analysed data obtained with larger nanodisc sizes by using higher amounts of lipids than described above. Although these larger nanodiscs were heterogeneous in size and cryo-EM analysis only yielded low resolution reconstructions, the ECF complex appears to adopt a similar conformation to the one observed with tighter nanodiscs (*SI Appendix,* Fig. S1 *B*).

This result shows that the size of the nanodisc does not dictate the observed structural features. To further rule out a potential artefact, we decided to collect data with ECF-FolT2 in detergent micelles, which are unconstraint by scaffold proteins. We obtained a good distribution of particles (*SI Appendix,* Fig. S6 *A,B*), and 2D class averages of particles extracted from around 700 movies also showed visible secondary structure elements, details within the detergent micelles, and distinct views corresponding to ECF-FolT2 (*SI Appendix,* Fig. S6 *C*). Despite the relatively small dataset,

we managed to obtain a reconstruction of ECF-FolT2 in detergent micelles at 3.4 Å resolution (*SI Appendix,* Fig. S7 *A*-*D*, Table S1). The structure of ECF-FolT2 in detergent micelles (*SI Appendix,* Fig. S8 *A*) is virtually identical to that of ECF-FolT2 in lipid nanodiscs (rmsd 0.77 Å, *SI Appendix,* Fig. S8 *B*), adopting the same inward-facing apo conformation. Altogether, this suggests that the surrounding environment has little influence on the structural conformation that ECF-FolT2 adopts. Analogously, the detergent micelle is not uniform in thickness either. Even though the detergent micelle is overall thicker than the nanodisc, it thins around to comparable thickness as the nanodiscs in the same locations where the bilayer of the nanodisc reaches its thinnest parts (*SI Appendix,* Fig. S8 *C*). Since the detergent micelle is not constrained by lateral forces of a scaffold protein, this result strongly indicates that the deformation of the surrounding environment, is mediated by the transporter itself. Consistently, the detergent molecules of the micelle adopt similar orientations as the lipid molecules of the lipid nanodisc in the vicinity of the protein.

Mechanistic and structural importance of protein-lipid interactions

The reconstitution of ECF-FolT2 into lipid nanodiscs also made it possible to analyse the protein-lipid interactions. Multiple non-protein densities were found around the membrane protein components of the complex (Fig. 3). The overall shape of the membrane embedded part of the complex is a highly asymmetrical, with a much larger footprint on the cytoplasmic side compared to the extracellular side. Most of the observed lipids densities are confined to the respective inner leaflet of the membrane (Fig. 3*A*-*C*). We interpreted the densities as annular phospholipids, whereby the precise identity (head group and acyl chains) remains ambiguous. Computational lipid fingerprint analysis indicated a preferred interaction of anionic lipids with the ECF transporter complex (5), and hence lipid densities were modelled where possible as phosphatidylglycerols. Based on their location, modelled lipids were grouped into 3 regions (Fig. 3*A*-*C*).

The first region corresponds to the cytoplasmic base of FolT2 that is facing the lipid environment (Fig. 3*A*). A lipid molecule (labelled I in Fig. 3*A*) was found sandwiched between the interface shared by FolT2 and EcfT, from which one of the acyl chains protrudes into the interface almost parallel to the lipid nanodisc while the other acyl chain wraps around TMH3 of FolT2. In this region an additional density is present (labelled I* in inset of Fig. 3*A*). It could be indicative for a second lipid molecule in this region, or represent a third acyl chain forming a cardiolipin molecule, which was suggested previously based on computational lipid finger printing analysis (5). Another lipid molecule could be resolved between TMH4 and TMH5 where one of the acyl chains lies within a narrow groove between TMH4 and TMH5 while the other is wrapped around the amino-terminal region of TMH5 (labelled II in Fig. 3*A*). The third lipid molecule was observed at the same height as the amino-terminal end of TMH5 between TMH6 and the amino-terminal region of coupling helix 3 in EcfT (labelled III in Fig. 3*A*). Notably, all three resolved lipids demark the boundary of the thinnest region of the lipid nanodisc and lie almost horizontal to the membrane plane, indicating that the observed thinning is caused by tilting of the lipid molecules. Additionally, the lipids are located near positively charged residues (*SI Appendix,* Fig. S5 *A* and S9 *A*). Similarly, a detergent molecule (*SI Appendix,* labelled as α in Fig. S9 *B*) and two potentially co-purified lipid molecules (*SI Appendix,* labelled as β and γ in Fig. S9 *B*) were observed in the same region with similar tilted orientations in the structure of ECF-FolT2 in detergent micelles. While the preferential occurrence of positively charged residues agrees with the positive-inside rule (23), this region was also suggested to provide binding sites for phosphatidylglycerols or cardiolipins (5).

The second region corresponds to the exit pathway for the substrate (Fig. 3*B*). A density corresponding to an acyl chain of a lipid is present at the amino-terminal part of coupling helix 2 in EcfT and the loop L1 of FolT2 (labelled IV in Fig. 3*B*), with the latter likely shielding the exit pathway from the hydrophobic milieu. A second density for a phospholipid acyl chain is sandwiched between two tryptophan residues near the pivot point of the domains of EcfT (labelled V in Fig. 3*B*). It might

help to stabilise the hydrophobic cleft that is formed by the kink in TMH3 of EcfT induced by the conserved Pro71.

The third region corresponds to the transmembrane helices of EcfT (Fig. 3*C*). Densities corresponding to acyl chains of lipids could be interpreted near a positively charged belt around the transmembrane helices of EcfT on the inner leaflet (labelled VI in Fig. 3*C*, *SI Appendix,* Fig. S9 *C*), while the only densities on the outer leaflet are found by the amino-terminal end of TMH4 and between TMH2 and TMH3 (labelled VII in Fig. 3*C*). Notably, all lipids in this region have a canonical orientation of the acyl chain (roughly perpendicular to the membrane plane), rather than the tilted orientation as in the region by the cytoplasmic base of FolT2 (Fig. 3*A*).

Discussion

ECF transporter complexes mediate the uptake of micronutrients such as vitamins and transition metals in bacteria. They have been proposed to operate by a bilayer-mediated toppling mechanism (5). Our work provides the first experimental evidence that ECF transporter complexes are likely to remodel the lipid bilayer in order to facilitate transport.

The cryo-EM reconstructions determined in lipid nanodiscs and detergent micelles demonstrate that the S-component assumes a toppled orientation in the inward-facing apo conformation irrespective of the surrounding environment. The structures also reveal a deformation and thinning of the surrounding environment and hints at the mechanistic and structural role of lipids. In the inward-open apo conformation, a thinning of the local environment occurs near the cytoplasmic base of the S-component, which is solvent exposed and overall positively charged. Lipid molecules are resolved in this region, highlighting the importance of specific interactions to maintain the boundary of the deformation. When replacing the model of ECF-FolT2 with the model of the pantothenate-specific ECF transporter complex (ECF-PanT, PDB: 6zg3), the positively charged cytoplasmic base of PanT also remains solvent exposed (*SI Appendix,* Fig. S9 D). It is likely that the deformation of the local environment provides the means to keep the highly positively charged cytoplasmic base of S-components solvent exposed when toppling within the membrane. Furthermore, it could also be important for the stabilisation of the inward-facing conformation together with the interaction formed with EcfA' (Fig. 1*D,E*). Notably, this region is resolved to the highest resolution in the cryo-EM reconstructions (*SI Appendix,* Fig. S3 *C* and S7 *C*). The thinning of the lipid nanodisc observed near the exit pathway for the transported substrate is likely a long-range effect caused by the deformation on the opposite side and in terms of biological membranes can be explained by the formation of an indentation in the local environment of the transporter. The remodelling of the local environment by thinning of the lipid bilayer and the protein-lipid interactions could provide a mechanism to reduce the energy barrier for the S-component to topple within the membrane in the transport cycle, and to create a pathway leading to the correct relative orientation of the ECF module and the S-component for docking.

We therefore extend the bilayer-mediated toppling mechanism by also considering the synergetic properties of the components in the ECF transporter complex (Fig. 4). The unengaged S-component in the outward-facing open conformation captures the substrate from the external environment. A freely available ECF module thins and bends the membrane locally, where it adopts a slightly tilted conformation (5). This conformation and local membrane thinning attract the substrate-bound S-component to dock and drive the toppling of the S-component within the membrane. (State 1 in Fig. 4). In the toppled state, the bound substrate is released into the cell. In this state, the S-component is tightly engaged with the ECF module stabilising the inward-facing conformation. At the same time, the local environment is deformed to ensure that the charged cytoplasmic base remains solvent exposed resulting in a further stabilisation of the inward-facing conformation (State 2 in Fig. 4). While the inward-facing apo-conformation represents a conformation that is stabilised by protein-protein interactions, the bilayer deformations observed in our structure may cause some strain. Binding and hydrolysis of ATP releases the empty S-

component and possibly relieves the strain, allowing the rotation of the S-component back to the outward-facing state so that in can engage in binding of a new substrate (State 3 in Fig. 4).

Small asymmetric membrane proteins with a molecular weight of 150 kDa or lower pose challenges for single-particle cryo-EM because of their inherently low signal-to-noise ratio and lack of contrast in vitreous ice. Imaging with 200-kV cryo-TEMs, or lower voltages, is gaining increasing prominence, in particular with membrane proteins. Especially small (membrane) proteins benefit from the increased image contrast originated from the higher elastic cross-section at lower acceleration voltages (25, 26). However, adequate ice thickness ranges are required to maximise the quality and efficacy of the output, especially at lower acceleration voltages, for which our improved data collection scheme based on prior sample thickness measurements has proven to be instrumental (19). The capabilities of 200-kV TEMs of reaching better than 3 Å resolution have been demonstrated by various groups with soluble proteins (27–33). Our work is a further demonstration that this can be also accomplished with a small asymmetric membrane protein. It is likely that a combination of the biochemistry, technical aspects and image processing contributed to achieve such a resolution in the end.

The influence of lipids and the deformation of the lipid bilayer on the function of membrane proteins is becoming increasingly acknowledged and has been highlighted in single-particle cryo-EM studies on the proteins belonging to the TMEM16 family (10, 11), the archaeal glutamate transporter homologs (12, 13), the human ER membrane protein complex (14), the β-barrel assembly machinery (15), the bacterial mechanosensitive channel of small conductance (16), and the human signal peptidase complex (17), to name a few. Our work overall provides experimentally the first glimpse on the bilayer-mediated toppling mechanism by single-particle cryo-EM, which allows the dynamic interaction of different S-components with the same ECF module. Moreover, it lays the foundations to further explore the influence of membrane deformations on the transport cycle in ECF transporter complexes within a near native environment. ECF transporter complexes have recently gained renewed attention with the identification of a novel haem transporter belonging to the family of ECF-type ABC transporters (34–36). As various ECF transporters complexes are encoded in the genome of various human pathogens but not in humans (37, 38), it makes them attractive targets for newly designed antimicrobial compounds, for which this work represents a stepping stone towards studying their means of action on a structural level.

Materials and Methods

Cloning, expression and membrane vesicle preparation

The cloning of ECF-FolT2 into the p2BAD expression vector was described previously(4). His10-ECF-FolT2-StrepII was expressed in *Escherichia coli* MC1061 cells as described previously with minor changes (4). Briefly, cells were grown in 5 L baffled-flasks containing 2 L 2xYT liquid medium supplemented with 2.5 mM potassium phosphate (KPi), pH 7.5, 0.5 % (v/v) glycerol, 100 µg/ml ampicillin and 200 µl/L Antifoam 204 (Sigma) at 37 °C with shaking at 200 rpm for 2 hours. The temperature was subsequently reduced to 25 °C and protein expression was induced at an OD_{600nm} of ~ 0.8 with 0.01 % (w/v) L-arabinose. Cells were harvested 3 hours post-induction (7500 x g, 15 min, 4 °C), washed in storage buffer (50 KPi, pH 7.5, 10 % (v/v) glycerol), and membrane vesicles prepared as previously described (4). Membrane vesicles were stored in aliquots containing 30 mg total protein as determined by a bicinchoninic acid assay kit (Thermo Fisher Scientific) at -80 °C after flash-freezing in liquid nitrogen.

Purification of ECF-FolT2

ECF-FolT2 was purified as described previously with minor changes to the protocol (4). Briefly, membrane vesicles containing 60 mg total protein were buffered in 50 mM KPi, pH 7.5, 300 mM NaCl, 1 % (w/v) n-dodecyl-b-D-maltopyranoside (DDM, Glycon), and solubilised for 1 hour at 4 °C at the lowest speed on a rotator. The solubilised sample was clarified by ultracentrifugation at 286,625 x g for 35 min and the supernatant was incubated with 0.5 ml Nickel-Sepharose 6 Fast

Flow beads (Cytiva) for 1 hour at 4 °C at the lowest speed on a rotator, which were previously equilibrated with wash buffer (50 mM KPi, pH 7.5, 300 mM NaCl, 50 mM imidazole, pH 8.0, 0.05 % (w/v) DDM). The suspension was packed into an empty polypropylene column (Bio-Rad), and the beads were washed with 30 column volumes wash buffer. Bound proteins were eluted with elution buffer (50 mM KPi, pH 7.5, 300 mM NaCl, 500 mM imidazole, pH 8.0, 0.04 % (w/v) DDM) in 250, 850 and 250 µl fractions. The second elution fraction was used for further purification by size-exclusion chromatography (SEC) using a Superose 6 Increase 10/300 GL column (Cytiva) equilibrated with SEC buffer (20 mM Tris, pH 8.0, 150 mM NaCl, 0.0261 % (w/v) DDM). Peak fractions containing ECF-FolT2 were pooled and used either for grid preparation or for reconstitution into lipid nanodiscs.

Reconstitution of ECF-FolT2 into lipid nanodiscs.
The reconstitution procedure was performed according to established protocols (18, 39). Briefly, *E. coli* polar lipid extracts (Avanti Polar Lipids) in chloroform were vacuum-dried and re-hydrated in 20 mM Tris, pH 8.0, 150 mM NaCl, 1.75 % (w/v) DDM to a concentration of 20 mg/ml. Freshly purified ECF-FolT2 from the size-exclusion chromatography step was mixed with purified MSP2N2 and lipids at a 1:5:250 molar ratio of ECF-FolT2 : MSP2N2 : lipids and kept on ice for 30 min, after which 200 mg/ml washed Bio-Beads SM-2 (Bio-Rad) was added and left to incubate at 4 °C on a rotator at the lowest speed. Another portion of 200 mg/ml Bio-Beads were added and left to incubate for 16 hours overnight. The reconstitution mixture was separated from the Bio-Beads, and incubated with 0.5 ml Nickel-Sepharose 6 Fast Flow beads for 1 hour at 4 °C at the lowest speed on a rotator, which were previously equilibrated with wash buffer (20 mM Tris, pH 8.0, 150 mM NaCl). The suspension was packed into an empty polypropylene column, and the beads were washed with 40 column volumes wash buffer. Bound proteins were eluted with elution buffer (20 mM Tris, pH 8.0, 150 mM NaCl, 500 mM imidazole, pH 8.0) in 250, 850 and 250 µl fractions. The second elution fraction was used for further purification by size-exclusion chromatography (SEC) using a Superose 6 Increase 10/300 GL column (Cytiva) equilibrated with SEC buffer (20 mM Tris, pH 8.0, 150 mM NaCl). Peak fractions containing the ECF-FolT2-MSP2N2-lipid complex were pooled and used for grid preparation.

Malachite Green Phosphate assay
The ATPase activity was determined using a commercially available Malachite Green Phosphate assay kit (Sigma). The reactions were prepared according to the manufacturer's instructions in volume of 100 µl. Briefly, the ATPase activity was allowed to proceed for 15 min at 30 °C with 0.5 µg nanodisc-embedded protein in SEC buffer (20 mM Tris, pH 8.0, 150 mM NaCl) supplemented either 200 µM Mg-ATP or 200 µM Mg-ADP or no adenine nucleotides. The reactions were stopped with 1.25 mM EDTA, pH 8.0, and 20 µl of the working solution from the Malachite Green Phosphate Assay Kit was added a reaction volume in 80 µl in 96-well plates. The colour was allowed to develop for 30 min at room temperature before measuring the ATPase activity at 640 nm with a TECAN Sparx plate reader. The measurement was performed as biological duplicate containing each technical triplicates. Phosphate concentrations were calculated from standard curves obtained with the supplied phosphate standard of the kit.

Cryo-EM sample preparation of ECF-FolT2 in DDM micelles and data acquisition
Prior to grid preparation, the sample was concentrated to 7.9 mg/ml with a 100 kDa MWCO centrifugal concentrator (Millipore), and used for immediately for grid preparation. Quantifoil Au R1.2/1.3 300 mesh and UltrAuFoil R1.2/1.3 300 mesh (Quantifoil) grids were glow-discharged (Edwards Scancoat 6) at 5 mA for 30 and 60 seconds, respectively. The sample was applied at a volume of 2.8 µl onto grids, which were blotted for 4 seconds after a wait time for 2.5 seconds using a Vitrobot Mark IV (Thermo Fisher Scientific) at 15 °C and 100 % humidity, subsequently plunge-frozen in a liquid ethane-propane mixture and stored in liquid nitrogen until use. Cryo-EM data were collected on a Talos Arctica microscope (Thermo Fisher Scientific) operating at 200-kV with a BioQuantum post-column energy filter (Gatan) in zero-loss mode, a 20-eV slit, and a 100 µm objective aperture, in an automated fashion with EPU version 1.12 (Thermo Fisher Scientific) on a

K2 Summit detector (Gatan) in counting mode. Movies were recorded at a physical pixel size of 1.012 Å (calibrated magnification of 49,407x), a defocus range from -0.8 to -1.8 µm, an exposure time of 9 seconds with a sub-frame exposure time of 150 ms (60 frames), and a total electron exposure on the specimen level of 53.3 electrons per $Å^2$. The best regions on the grid for data acquisition were screened and selected with an in-house written script to calculate the ice thickness (19), which was set between 20 and 40 nm, and the data quality was monitored on-the-fly using the software FOCUS version 1.0.0 (40).

Image processing and model building of ECF-FolT2 in DDM micelles

A total of 464 and 357 dose-fractioned cryo-EM images were recorded back-to-back from the Quantifoil (dataset 1) and UltrAuFoil (dataset 2) grids (frozen at the same time with protein from the same purification), respectively, and subjected to motion correction and dose weighting of frames in MotionCor2 version 1.2.1 (41). The CTF parameters were estimated on the movie frames with CTFFIND4.1.13 (42). Low quality images were removed on the basis of visual inspection of the images showing contamination or poor CTF estimation, and a total of 443 and 265 images remained for further processing from dataset 1 and 2, respectively. MotionCor2 and CTFFIND4 were used within the FOCUS software. Particles were picked with crYOLO version 1.2.2 using the PhosaurusNet architecture with anchors set to 160 (43). A model was created and trained on 8 and 3 micrographs from dataset 1 and 2, respectively, which was subsequently used for picking on all images. A total of 75,688 and 85,775 particles were picked from dataset 1 and 2, respectively, and imported into RELION version 3.0.7 (44). Particles from each set were extracted separately using a box size of 256 pixels, which were subjected to three rounds of 2D classification with a particle mask diameter of 200 Å and the expectation step limited to 10 Å resolution, after which particles from both data sets were combined and three additional rounds of 2D classification was performed. A robust classification of the extracted particles was achieved by ignoring the effects of the CTF until the first zero transition in all 2D classification rounds. A final 2D classification step was performed without ignoring the effects of the CTF until the first zero transition. 2D classes that showed high-resolution features were selected (73,900 particles) for 3D auto-refinement into a single consensus map using an initial model generated *de novo* by Stochastic Gradient Descent (SGD) method in RELION and lowpass filtered to 60 Å. The overall resolution of the consensus map after post-processing was 3.81 Å resolution. The overall resolution was improved to 3.76 Å of the best 3D class (52,109 particles) after 3D classification into four classes. The resolution was further improved to 3.70 Å after CTF refinement. Particles were subjected to Bayesian polishing (45) after obtaining optimal parameters (s_vel: 0.7995, s_div 5190, s_acc 5.46) yielding a map at 3.55 Å resolution. Another round of CTF refinement improved the resolution to 3.45 Å resolution. The resolution dropped even further after removing particles with a CtfMaxResolution below 4 Å resolution using the subset selection option, yielding a final map containing 41,963 particles at 3.41 Å resolution. All reported resolutions were estimated with the 0.143 cut-off criterion (46) with gold-standard Fourier-shell correlation (FSC) between two independently refined half maps (47). During post-processing, high resolution noise substitution was used to correct for convolution effects of real-space masking on the FSC curve (48). The directional resolution anisotropy of density maps was quantitatively evaluated using the remote 3DFSC processing server (accessible at https://3dfsc.salk.edu) (49). Local resolution variations were estimated with RELION. The data collection and processing parameters are summarised in Table S1. The final map was sharpened with LocalDeblur (50) using the local resolution map estimated with MonoRes (51) through Scipion version 2.0 (52). Initially, individual chains from the crystal structure of ECF-FolT2 in the apo state (PDB: 5jsz) was fitted into density of the sharpened map in UCSF Chimera version 1.14 (53). The entire model was subsequently adjusted and improved in COOT version 0.9-pre (54). Residues for amino acids 1,15-16 and 282 in EcfA, amino acids 1, 13-21, 283-287 in EcfA', amino acids 1-9 in FolT2, and amino acids 1-6 in EcfT could not be place due to poor or absent densities. In EcfA, amino acid 1 was modelled as a glycine, which is part of the TEV cleavable deca-histidine affinity tag and replaces the starting methionine at that position. Two residues of the STREPII affinity at the carboxy-terminal end of FolT2 could be modelled also modelled. The model was subjected to

an iterative process of real space refinement against the postprocessed map in PHENIX version 1.18-3861 (55). All programs used for image processing were accessed through SBGrid (56).

Cryo-EM sample preparation of ECF-FolT2 embedded in lipid nanodiscs and data acquisition

Prior to grid preparation, nanodisc-embedded ECF-FolT2 used for the inward-facing apo conformation was concentrated to 7.9 mg/ml with a 100 kDa MWCO centrifugal concentrator, and then used immediately for grid preparation. Quantifoil Au R1.2/1.3 300 mesh grids were glow-discharged at 5 mA for 30 seconds. Prior to sample application, fluorinated Fos-choline 8 (Anatrace) was added to a final concentration of 2.9 mM to obtain an even distribution of well separated particles. The sample was immediately applied at a volume of 2.8 µl onto grids, blotted for 3 – 4 seconds using the Vitrobot at 15 °C and 100 % humidity, and subsequently flash-frozen in a liquid ethane-propane mixture and stored in liquid nitrogen until use. Cryo-EM data were collected as described above with minor changes as follows. Data were collected in an automated fashion with EPU version 2.4 (Thermo Fisher Scientific). The detector was operating in super-resolution mode with movies recorded at a physical pixel size of 0.771 Å (calibrated magnification of 64,851x), a defocus range from -0.8 to -1.8 µm, an exposure time of 9 seconds with a sub-frame exposure time of 150 ms (60 frames), and a total electron exposure on the specimen level of 51.1 electrons per $Å^2$. As a result of adding fluorinated Fos-choline 8, the ice thickness script was adjusted to 30 and 50 nm to obtain the best regions on the grid for data acquisition.

Image processing and model building of ECF-FolT2 embedded in lipid nanodiscs

A total of 4722 movies were collected from four grids (frozen at the same time with protein from the same purification) in three sessions over the course of three months, and subjected to gain correction, Fourier cropping by a factor of two, motion correction and dose weighting of frames in MotionCor2. The CTF parameters were estimated on the movie frames with CTFFIND4. Low quality images were removed on the basis of visual inspection of the images showing contamination or poor CTF estimation, and a total of 3974 movies remaining for further processing. Particles were picked with crYOLO version 1.5.0 using the PhosaurusNet architecture with anchors set to 180. A picking model was created and trained on 10 micrographs, which was subsequently used for picking on all images. A total of 1,362,547 particles were picked and imported into the beta-release of RELION version 3.1 (57). Particles were extracted with a box size of 320 px and downscaled initially to 3.084 Å/px, which were then subjected to 4 rounds of 2D classification with a particle mask diameter of 180 Å with the expectation step gradually increased from 10 Å to 6 Å in each step. A robust classification of the extracted particles was achieved by ignoring the effects of the CTF until the first zero transition in all 2D classification rounds. Resulting 2D classes displaying high-resolution features were selected (658,218 particles) for 3D classification into three classes using an initial model generated *de novo* by the SGD method in RELION and lowpass filtered to 60 Å. The particles from the best class (392,698 particles) were re-extracted and re-centred with a box size of 320 pixels without downscaling, which were subjected to 3D auto-refinement resulting in a reconstruction at 3.16 Å resolution after post-processing with the resolution not improving after a round of CTF refinement (beam-tilt estimation, per-particle defocus and per-micrograph astigmatism). The resolution however improved beyond 3 Å after Bayesian polishing with default parameters and CTF refinement (beam-tilt estimation, per-particle defocus and per-micrograph astigmatism) to 2.94 Å. Particles from the best class (282,236 particles) after 3D classification (tau_fudge = 8, E-step limit = 6 Å) using a soft mask (4 pixel extension, 8 pixel soft cosine edge) without image alignment into three classes, and CTF refinement (beam-tilt estimation, per-particle defocus and per-micrograph astigmatism) resulted in a reconstruction at 2.87 Å resolution. Another round of Bayesian polishing with particles re-extracted with a box size of 386 pixels resulted in a small improvement to 2.85 Å resolution. CTF refinement (trefoil estimation, anisotropic magnification estimation, beam-tilt estimation, per-particle defocus and per-micrograph astigmatism) yielded a reconstruction at 2.74 Å resolution. Particles from the best class (166,524 particles) of a final round of 3D classification (tau_fudge = 12, E-step limit = 6 Å) using a soft mask around the protein density (4 pixel extension, 8 pixel soft cosine edge) without image alignment

into three classes and two rounds of CTF refinement trefoil estimation, anisotropic magnification estimation, beam-tilt estimation, per-particle defocus and per-micrograph astigmatism) resulted in a final reconstruction at 2.69 Å resolution. All reported resolutions were estimated as described above and local resolution variations for both maps were estimated with RELION. Directional anisotropy was evaluated as described above. The data collection and processing parameters are summarised in Table S1. The final map was sharpened as described above. The model from the cryo-EM structure of ECF-FolT2 in DDM micelles was fitted into the density in Chimera after which the model was subsequently adjusted and improved in COOT. Residues for amino acids 1,15-16 and 282 in EcfA, amino acids 1, 12-20, 283-287 in EcfA', amino acids 1-9 in FolT2, and amino acids 1-4 in EcfT could not be placed due to poor or absent densities. Water molecules were added to the model using phenix.douse as part of the PHENIX programme, which were manually curated and retained based on logical interaction geometries and clear and visible densities. The model was subjected to an iterative process of real space refinement against the postprocessed map in PHENIX. All programs used for image processing were accessed through SBGrid.

Structure validation

The quality of the fit was validated by a Fourier shell cross correlation (FSCsum) between the refined model and the final map. To monitor the effects of potential overfitting, random shifts (up to 0.5 Å) were introduced into the coordinates of the final model, followed by refinement against the first unfiltered half map. The FSC between this shaken-refined model and the first half map used during validation refinement is termed FSCwork, and the FSC against the second half map, which was not used at any point during refinement, is termed FSCfree. A marginal gap between the curves describing FSCwork and FSCfree indicates no overfitting of the model. The chemo-physical properties of the final model were validated by MolProbity (58).

Figure preparation

Figures were prepared with Pymol version 2.4.1 (The PyMOL Molecular Graphics System, Schrödinger, LLC), Chimera and UCSF ChimeraX version 1.1 (22). Final illustrations were prepared with Affinity Designer version 1.8.6 (Serif (Europe) Ltd).

Data availability

Data supporting the findings of this manuscript are available from the corresponding authors upon request. Cryo-EM density maps, half-maps and masks of ECF-FolT2 in DDM micelles and MSP2N2 lipid nanodiscs have been deposited in the Electron Microscopy Data Bank (EMDB) under accession numbers EMD-12483 and EMD-12484, respectively. The respective atomic models are available through the Protein Data Bank under the PDB accession codes 7NNT (ECF-FolT2 in DDM micelles) and 7NNU (ECF-FolT2 in MSP2N2 lipid nanodiscs).

Acknowledgments

We thank A.A. Garaeva for freezing grids of ECF-FolT2 in detergent micelles, G.T. Oostergetel for help with initial cryo-EM data acquisition, and M. Punter for maintenance of the image processing cluster. As part of the COFUND project oLife, C.T. acknowledges funding from the European Union's Horizon 2020 research and innovation program under the grant agreement No. 847675. C.P. acknowledges funding from the Dutch Research Council: NWO Veni grant 722.017.001 and NWO Start-Up grant 740.018.016. D.J.S. acknowledges funding from the Dutch Research Council: NWO TOP grant 714.018.003.

References

1. C. Thomas, R. Tampé, Structural and Mechanistic Principles of ABC Transporters. *Annu.*

Rev. Biochem. **89**, 605–636 (2020).

2. S. Rempel, W. K. Stanek, D. J. Slotboom, ECF-Type ATP-Binding Cassette Transporters. *Annu. Rev. Biochem.* **88**, 551–576 (2019).

3. I. Setyawati, *et al.*, In vitro reconstitution of dynamically interacting integral membrane subunits of energy-coupling factor transporters. *eLife* **9**, e64389 (2020).

4. L. J. Y. M. Swier, A. Guskov, D. J. Slotboom, Structural insight in the toppling mechanism of an energy-coupling factor transporter. *Nat Commun* **7**, 11072 (2016).

5. I. Faustino, *et al.*, Membrane mediated toppling mechanism of the folate energy coupling factor transporter. *Nat Commun* **11**, 1763 (2020).

6. J. A. Santos, *et al.*, Functional and structural characterization of an ECF-type ABC transporter for vitamin B12. *eLife* **7**, e35828 (2018).

7. T. Wang, *et al.*, Structure of a bacterial energy-coupling factor transporter. *Nature* **497**, 272–276 (2013).

8. K. Xu, *et al.*, Crystal structure of a folate energy-coupling factor transporter from Lactobacillus brevis. *Nature* **497**, 268–271 (2013).

9. M. Zhang, *et al.*, Structure of a pantothenate transporter and implications for ECF module sharing and energy coupling of group II ECF transporters. *Proceedings of the National Academy of Sciences* **111**, 18560–18565 (2014).

10. V. Kalienkova, *et al.*, Stepwise activation mechanism of the scramblase nhTMEM16 revealed by cryo-EM. *eLife* **8**, e44364 (2019).

11. M. E. Falzone, *et al.*, Structural basis of Ca2+-dependent activation and lipid transport by a TMEM16 scramblase. *eLife* **8**, e43229 (2019).

12. V. Arkhipova, A. Guskov, D. J. Slotboom, Structural ensemble of a glutamate transporter homologue in lipid nanodisc environment. *Nat Commun* **11**, 998 (2020).

13. X. Wang, O. Boudker, Large domain movements through the lipid bilayer mediate substrate release and inhibition of glutamate transporters. *eLife* **9**, e58417 (2020).

14. T. Pleiner, *et al.*, Structural basis for membrane insertion by the human ER membrane protein complex. *Science* **369**, 433 (2020).

15. M. G. Iadanza, *et al.*, Distortion of the bilayer and dynamics of the BAM complex in lipid nanodiscs. *Commun Biol* **3**, 766 (2020).

16. Y. Zhang, *et al.*, Visualization of the mechanosensitive ion channel MscS under membrane tension. *Nature* **590**, 509–514 (2021).

17. A. M. Liaci, *et al.*, “Structure of the Human Signal Peptidase Complex Reveals the Determinants for Signal Peptide Cleavage” (2020).

18. Y. V. Grinkova, I. G. Denisov, S. G. Sligar, Engineering extended membrane scaffold proteins for self-assembly of soluble nanoscale lipid bilayers. *Protein Engineering Design and Selection* **23**, 843–848 (2010).

19. J. Rheinberger, G. Oostergetel, G. P. Resch, C. Paulino, Optimized cryo-EM data-

acquisition workflow by sample-thickness determination. *Acta Crystallogr D Struct Biol* **77**, 565–571 (2021).

20. G. B. Erkens, *et al.*, The structural basis of modularity in ECF-type ABC transporters. *Nature Structural & Molecular Biology* **18**, 755–760 (2011).

21. R. P.-A. Berntsson, *et al.*, Structural divergence of paralogous S components from ECF-type ABC transporters. *Proceedings of the National Academy of Sciences* **109**, 13990–13995 (2012).

22. T. D. Goddard, *et al.*, UCSF ChimeraX: Meeting modern challenges in visualization and analysis: UCSF ChimeraX Visualization System. *Protein Science* **27**, 14–25 (2018).

23. G. Heijne, Y. Gavel, Topogenic signals in integral membrane proteins. *Eur J Biochem* **174**, 671–678 (1988).

24. D. A. Rodionov, *et al.*, A Novel Class of Modular Transporters for Vitamins in Prokaryotes. *JB* **191**, 42–51 (2009).

25. M. J. Peet, R. Henderson, C. J. Russo, The energy dependence of contrast and damage in electron cryomicroscopy of biological molecules. *Ultramicroscopy* **203**, 125–131 (2019).

26. R. Henderson, The potential and limitations of neutrons, electrons and X-rays for atomic resolution microscopy of unstained biological molecules. *Quarterly reviews of biophysics* **28**, 171–193 (1995).

27. M. A. Herzik, M. Wu, G. C. Lander, Achieving better-than-3-Å resolution by single-particle cryo-EM at 200 keV. *Nature Methods* **14**, 1075–1078 (2017).

28. M. A. Herzik, M. Wu, G. C. Lander, High-resolution structure determination of sub-100 kDa complexes using conventional cryo-EM. *Nat Commun* **10**, 1032 (2019).

29. M. Wu, G. C. Lander, M. A. Herzik, Sub-2 Angstrom resolution structure determination using single-particle cryo-EM at 200 keV. *Journal of Structural Biology: X* **4**, 100020 (2020).

30. F. Hamdi, *et al.*, 2.7 Å cryo-EM structure of vitrified M. musculus H-chain apoferritin from a compact 200 keV cryo-microscope. *PLoS ONE* **15**, e0232540 (2020).

31. A. Merk, *et al.*, 1.8 Å resolution structure of β-galactosidase with a 200 kV CRYO ARM electron microscope. *IUCrJ* **7** (2020).

32. B. J. Greber, *et al.*, The cryoelectron microscopy structure of the human CDK-activating kinase. *Proc Natl Acad Sci USA* **117**, 22849–22857 (2020).

33. B. J. Greber, J. Remis, S. Ali, E. Nogales, 2.5 Å-resolution structure of human CDK-activating kinase bound to the clinical inhibitor ICEC0942. *Biophysical Journal* **120**, 677–686 (2021).

34. A. Jochim, *et al.*, An ECF-type transporter scavenges heme to overcome iron-limitation in Staphylococcus lugdunensis. *eLife* **9**, e57322 (2020).

35. N. Chatterjee, *et al.*, A Novel Heme Transporter from the Energy Coupling Factor Family Is Vital for Group A Streptococcus Colonization and Infections. *J. Bacteriol.* **202**, e00205-20 (2020).

36. E. Verplaetse, *et al.*, Heme Uptake in Lactobacillus sakei Evidenced by a New Energy

Coupling Factor (ECF)-Like Transport System. *Appl. Environ. Microbiol.* **86**, e02847-19 (2020).

37. S. Bousis, I. Setyawati, E. Diamanti, D. J. Slotboom, A. K. H. Hirsch, Energy-Coupling Factor Transporters as Novel Antimicrobial Targets. *Advanced Therapeutics* **2**, 1800066 (2019).

38. B. Zhu, *et al.*, Genome-wide identification of Streptococcus sanguinis fitness genes in human serum and discovery of potential selective drug targets. *Molecular Microbiology* **n/a** (2020).

39. T. K. Ritchie, *et al.*, "Reconstitution of Membrane Proteins in Phospholipid Bilayer Nanodiscs" in *Methods in Enzymology*, (Elsevier, 2009), pp. 211–231.

40. N. Biyani, *et al.*, Focus: The interface between data collection and data processing in cryo-EM. *Journal of Structural Biology* **198**, 124–133 (2017).

41. S. Q. Zheng, *et al.*, MotionCor2: anisotropic correction of beam-induced motion for improved cryo-electron microscopy. *Nature Methods* **14**, 331–332 (2017).

42. A. Rohou, N. Grigorieff, CTFFIND4: Fast and accurate defocus estimation from electron micrographs. *Journal of Structural Biology* **192**, 216–221 (2015).

43. T. Wagner, *et al.*, SPHIRE-crYOLO is a fast and accurate fully automated particle picker for cryo-EM. *Commun Biol* **2**, 218 (2019).

44. J. Zivanov, *et al.*, New tools for automated high-resolution cryo-EM structure determination in RELION-3. *eLife* **7**, e42166 (2018).

45. J. Zivanov, T. Nakane, S. H. W. Scheres, A Bayesian approach to beam-induced motion correction in cryo-EM single-particle analysis. *IUCrJ* **6**, 5–17 (2019).

46. P. B. Rosenthal, R. Henderson, Optimal Determination of Particle Orientation, Absolute Hand, and Contrast Loss in Single-particle Electron Cryomicroscopy. *Journal of Molecular Biology* **333**, 721–745 (2003).

47. S. H. Scheres, S. Chen, Prevention of overfitting in cryo-EM structure determination. *Nature methods* **9**, 853–854 (2012).

48. S. Chen, *et al.*, High-resolution noise substitution to measure overfitting and validate resolution in 3D structure determination by single particle electron cryomicroscopy. *Ultramicroscopy* **135**, 24–35 (2013).

49. Y. Z. Tan, *et al.*, Addressing preferred specimen orientation in single-particle cryo-EM through tilting. *Nat Methods* **14**, 793–796 (2017).

50. E. Ramírez-Aportela, *et al.*, Automatic local resolution-based sharpening of cryo-EM maps. *Bioinformatics* **36**, 765–772 (2020).

51. J. L. Vilas, *et al.*, MonoRes: Automatic and Accurate Estimation of Local Resolution for Electron Microscopy Maps. *Structure* **26**, 337-344.e4 (2018).

52. J. M. de la Rosa-Trevín, *et al.*, Scipion: A software framework toward integration, reproducibility and validation in 3D electron microscopy. *Journal of Structural Biology* **195**, 93–99 (2016).

53. E. F. Pettersen, *et al.*, UCSF Chimera--A visualization system for exploratory research and analysis. *J. Comput. Chem.* **25**, 1605–1612 (2004).

54. P. Emsley, K. Cowtan, Coot: model-building tools for molecular graphics. *Acta Crystallogr D Biol Crystallogr* **60**, 2126–2132 (2004).

55. D. Liebschner, *et al.*, Macromolecular structure determination using X-rays, neutrons and electrons: recent developments in *Phenix*. *Acta Crystallogr D Struct Biol* **75**, 861–877 (2019).

56. A. Morin, *et al.*, Collaboration gets the most out of software. *eLife* **2**, e01456 (2013).

57. J. Zivanov, T. Nakane, S. H. W. Scheres, Estimation of high-order aberrations and anisotropic magnification from cryo-EM data sets in *RELION* -3.1. *IUCrJ* **7**, 253–267 (2020).

58. C. J. Williams, *et al.*, MolProbity: More and better reference data for improved all-atom structure validation: PROTEIN SCIENCE.ORG. *Protein Science* **27**, 293–315 (2018).

Figures

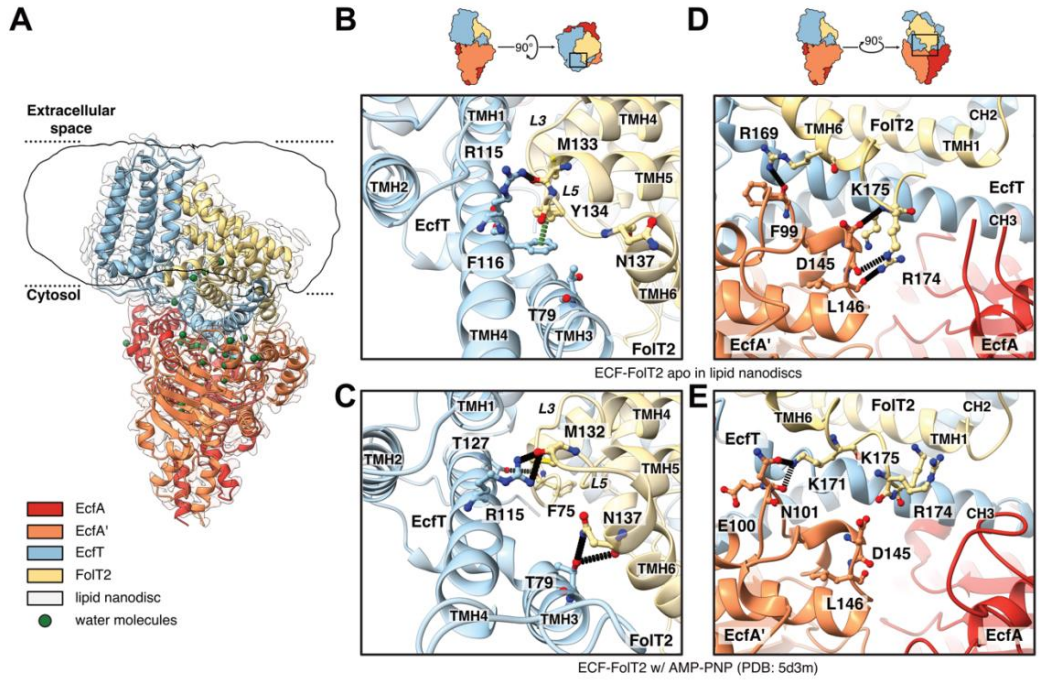

Figure 1. Cryo-EM structure of the folate-specific ECF transporter complex in the inward-facing apo conformation embedded in lipid nanodiscs. (*A*) Atomic model of ECF-FolT2 in lipid nanodiscs as viewed from the membrane plane shown in cartoon representation built into the cryo-EM density map (transparent contours at 9.5 σ) with an overlay of the density corresponding to the lipid nanodisc drawn transparent (unsharpened map low pass filtered to 6 Å and contoured at 0.325 σ). The two nucleotide-binding proteins (EcfA in red, EcfA' in orange) and the two membrane-embedded proteins (EcfT in blue, FolT2 in yellow) form together ECF-FolT2. Water molecules shown as green spheres. Approximate boundaries of the membrane are indicated by black dotted lines. (*B*-*E*) Interactions of the S-component with EcfT and EcfA'. Interactions formed between FolT2 to EcfT in the cryo-EM structure (*B*) and in the AMP-PNP-bound X-ray crystal structure of ECF-FolT2 (PDB: 5d3m) (*C*). Interactions formed between FolT2 to EcfA' in the cryo-EM structure (*D*) and in the AMP-PNP-bound structure (*E*). Individual polypeptides are coloured as in (*A*). Highlighted residues are represented in the ball-and-stick style. Hydrogen bonds and π-interactions are shown as black and green dotted lines. Selected structural elements and residues are labels. Schematic representations above panels (*B,D*) indicate the zoomed in regions for panels below.

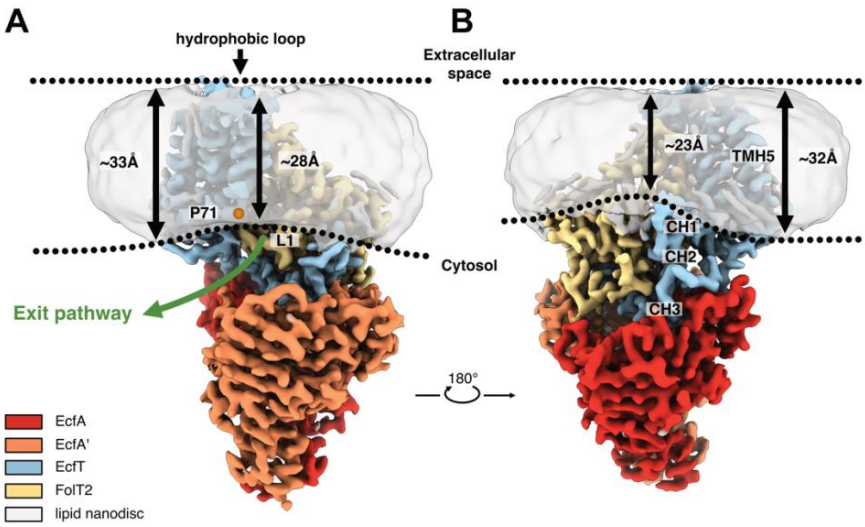

Figure 2. Membrane deformations mediated by ECF-FolT2. Densities for cryo-EM maps displayed as described in Fig. 1. (*A*) Viewed from the membrane plane on the side of the exit pathway for folate from the cavity in FolT2. The exit pathway is indicated by a green arrow. The pivot point of the membrane and coupling domains of EcfT at conserved residue Pro71 in THM3 is indicated by an orange sphere. (*B*) Viewed from the membrane plane as in (*A*) but rotated by 180° highlighting the deformation of the lipid nanodisc at the cytoplasmic base of FolT2. The approximate thickness of the lipid nanodiscs was determined using Chimera X (22) and indicated by black arrows. Selected structural elements are labelled. Approximate boundaries of the membrane are indicated by black dotted lines.

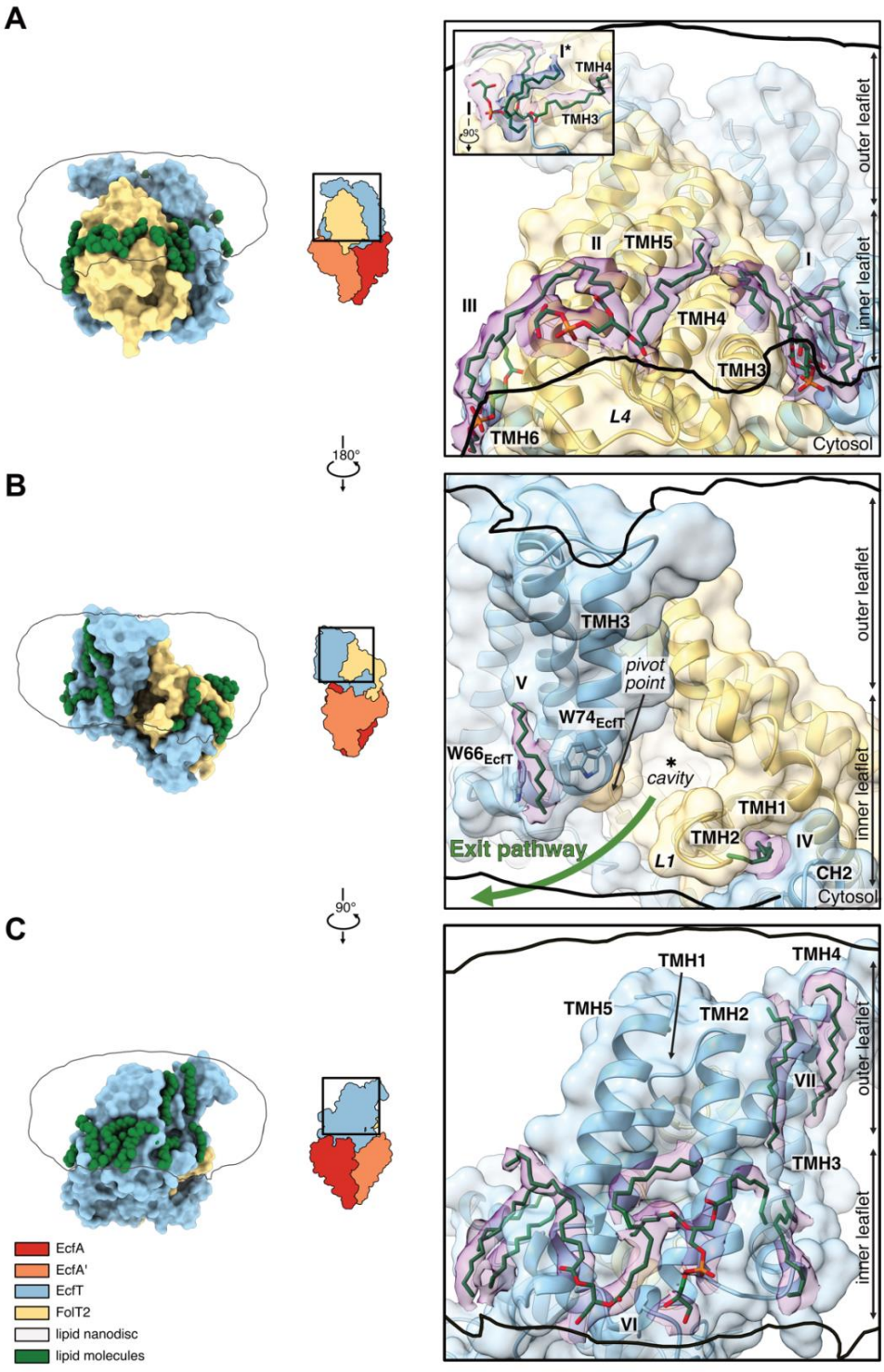
A
B
C
180°
90°
I*
TMH4
I
TMH3
90°
II
TMH5
I
III
TMH4
TMH3
L4
TMH6
Cytosol
outer leaflet
inner leaflet
TMH3
V
pivot
point
W74EcfT
W66EcfT
*
cavity
TMH1
TMH2
IV
Exit pathway
L1
CH2
Cytosol
outer leaflet
inner leaflet
TMH1
TMH4
TMH5
TMH2
VII
TMH3
VI
outer leaflet
inner leaflet
EcfA
EcfA'
EcfT
FolT2
lipid nanodisc
lipid molecules

Figure 3. Protein-lipid interactions. (*A*) Lipids at the cytoplasmic base of FolT2. The inset is a zoomed view of the large boxed panel rotated by 90°, highlighting the density (blue) for another acyl chain (labelled I*), which either belongs to a second lipid molecule in this region or forms with the remaining density of lipid I (purple density) a cardiolipin molecule. (*B*) Lipids near the exit pathway for the substrate. (*C*) Lipids around EcfT viewed from the membrane plane. Global views of the interpreted lipids (green spheres) around the membrane components EcfT and FolT2 (surface representation) within the lipid nanodisc (contoured as above) as viewed from the membrane plane are shown next to schematic representations of the full complex. Large boxed panels represent zoomed views of regions as highlighted in the schematic representations. Proteins are shown in cartoon and surface representation. Modelled lipids are shown in stick representation (green) with the corresponding cryo-EM density contoured at 6.5 σ (purple). Roman numbers in the panel represent individual lipids or lipid groups referred to in the main text. Selected structural elements are labelled. The contours of the lipid nanodisc (unsharpened map low pass filtered to 6 Å and contoured at 0.325 σ) are indicated in black. The exit pathway in (*B*) is indicated by a green arrow, and the inner and outer leaflet of the membrane are indicated by double-headed arrows (*A*-*C*). In all representations, proteins are coloured according to Fig. 1.

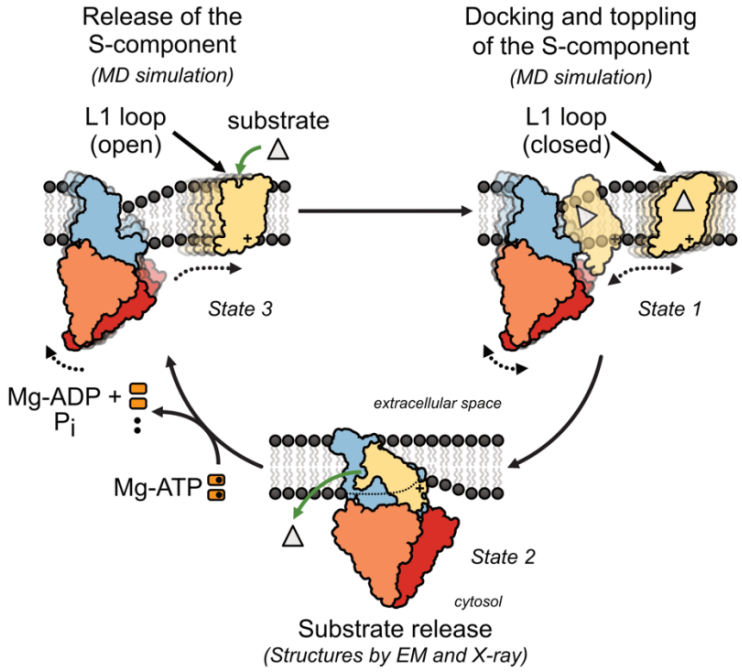

Figure 4. Substrate transport by a bilayer-mediated toppling mechanism of ECF transporter complexes. Schematic representation of the different states of the transport cycle by ECF transporter complexes with exchangeable S-components (so-called group II ECF transporters) (24). State 1: The substrate-bound S-component docks to a freely available ECF module, which is in a slightly tiled conformation and thins and bends the membrane. The S-component topples within the membrane. State 2: The ECF transporter complex assumes the inward-facing apo conformation, in which the bound substrate is released into the cell. The S-component locally deforms the membrane by which the positively charged base of the FolT2 remains solvent exposed. State 3: Binding and hydrolysis of Mg-ATP results in the rotation of the apo S-component to the outward-facing conformation and the release from the ECF module for renewed substrate binding. The ECF module tilts and bends the membrane for binding a substrate-bound S-component. State 3 is based on structural evidence by cryo-EM (this work) and X-ray crystallographic studies. The remaining states are based on molecular dynamics simulations (5).